

## Probing dense baryon-rich matter with virtual photons

Adamczewski-Musch, J.; Arnold, O.; Behnke, C.; Belounnas, A.; Belyaev, A.; Berger-Chen, J. C.; Biernat, J.; Blanco, A.; Blume, C.; Böhmer, M.; Bordalo, P.; Chernenko, S.; Chlad, L.; Deveaux, C.; Dreyer, J.; Dybczak, A.; Epple, E.; Fabbietti, L.; Fateev, O.; Filip, P.; Fonte, P.; Franco, C.; Friese, J.; Fröhlich, I.; Galatyuk, T.; Garzon, J. A.; Gernhäuser, R.; Golubeva, M.; Greifenhagen, R.; Guber, F.; Gumberidze, M.; Harabasz, S.; Heinz, T.; Hennino, T.; Hlavac, S.; Höhne, C.; Holzmann, R.; Ierusalimov, A.; Ivashkin, A.; Kämpfer, B.; Karavicheva, T.; Kardan, B.; Koenig, I.; Koenig, W.; Kolb, B. W.; Korcyl, G.; Kornakov, G.; Kotte, R.; Kühn, W.; Kugler, A.; Kunz, T.; Kurepin, A.; Kurilkin, A.; Kurilkin, P.; Ladygin, V.; Lalik, R.; Lapidus, K.; Lebedev, A.; Lopes, L.; Lorenz, M.; Mahmoud, T.; Maier, L.; Mangiarotti, A.; Markert, J.; Maurus, S.; Metag, V.; Michel, J.; Mihaylov, D. M.; Morozov, S.; Müntz, C.; Münzer, R.; Naumann, L.; Nowakowski, K. N.; Palka, M.; Parpottas, Y.; Pechenov, V.; Pechenova, O.; Petukhov, O.; Pietraszko, J.; Przygoda, W.; Ramos, S.; Ramstein, B.; Reshetin, A.; Rodriguez-Ramos, P.; Rosier, P.; Rost, A.; Sadovsky, A.; Salabura, P.; Scheib, T.; Schuldes, H.; Schwab, E.; Scozzi, F.; Seck, F.; Sellheim, P.; Siebenson, J.; Silva, L.; Sobolev, Y. G.; Spataro, S.; Ströbele, H.; Stroth, J.; Strzempek, P.; Sturm, C.; Svoboda, O.; Szala, M.; Tlusty, P.; Traxler, M.; Tsertos, H.; Usenko, E.; Wagner, V.; Wendisch, C.; Wiebusch, M. G.; Wirth, J.; Zanevsky, Y.; Zumbach, P.;

Originally published:

July 2019

**Nature Physics 15(2019), 1040-1045**

DOI: <https://doi.org/10.1038/s41567-019-0583-8>

Perma-Link to Publication Repository of HZDR:

<https://www.hzdr.de/publications/Publ-28909>

Release of the secondary publication  
on the basis of the German Copyright Law § 38 Section 4.

# Probing dense baryon-rich matter with virtual photons

J. Adamczewski-Musch<sup>4</sup>, O. Arnold<sup>10,9</sup>, C. Behnke<sup>8</sup>, A. Belounnas<sup>15</sup>, A. Belyaev<sup>7</sup>, J.C. Berger-Chen<sup>10,9</sup>, J. Biernat<sup>3</sup>, A. Blanco<sup>2</sup>, C. Blume<sup>8</sup>, M. Böhmer<sup>10</sup>, P. Bordalo<sup>2</sup>, S. Chernenko<sup>7</sup>, L. Chlad<sup>16</sup>, C. Deveaux<sup>11</sup>, J. Dreyer<sup>6</sup>, A. Dybczak<sup>3</sup>, E. Eppe<sup>10,9</sup>, L. Fabbietti<sup>10,9</sup>, O. Fateev<sup>7</sup>, P. Filip<sup>1</sup>, P. Fonte<sup>2,a</sup>, C. Franco<sup>2</sup>, J. Friese<sup>10</sup>, I. Fröhlich<sup>8</sup>, T. Galatyuk<sup>5,4</sup>, J. A. Garzón<sup>17</sup>, R. Gernhäuser<sup>10</sup>, M. Golubeva<sup>12</sup>, R. Greifeuhagen<sup>6,c</sup>, F. Guber<sup>12</sup>, M. Gumberidze<sup>5,b</sup>, S. Harabasz<sup>5,3</sup>, T. Heinz<sup>4</sup>, T. Hennino<sup>15</sup>, S. Hlavac<sup>1</sup>, C. Höhne<sup>11</sup>, R. Holzmann<sup>4</sup>, A. Ierusalimov<sup>7</sup>, A. Ivashkin<sup>12</sup>, B. Kämpfer<sup>6,c</sup>, T. Karavicheva<sup>12</sup>, B. Kardan<sup>8</sup>, I. Koenig<sup>4</sup>, W. Koenig<sup>4</sup>, B. W. Kolb<sup>4</sup>, G. Korcyl<sup>3</sup>, G. Kornakov<sup>5</sup>, R. Kotte<sup>6</sup>, W. Kühn<sup>11</sup>, A. Kugler<sup>16</sup>, T. Kunz<sup>10</sup>, A. Kurepin<sup>12</sup>, A. Kurilkin<sup>7</sup>, P. Kurilkin<sup>7</sup>, V. Ladygin<sup>7</sup>, R. Lalik<sup>10,9</sup>, K. Lapidus<sup>10,9</sup>, A. Lebedev<sup>13</sup>, L. Lopes<sup>2</sup>, M. Lorenz<sup>8</sup>, T. Mahmoud<sup>11</sup>, L. Maier<sup>10</sup>, A. Mangiarotti<sup>2</sup>, J. Markert<sup>4</sup>, S. Maurus<sup>10</sup>, V. Metag<sup>11</sup>, J. Michel<sup>8</sup>, D.M. Mihaylov<sup>10,9</sup>, S. Morozov<sup>12,d</sup>, C. Müntz<sup>8</sup>, R. Münzer<sup>10,9</sup>, L. Naumann<sup>6</sup>, K. N. Nowakowski<sup>3</sup>, M. Palka<sup>3</sup>, Y. Parpottas<sup>14,e</sup>, V. Pechenov<sup>4</sup>, O. Pechenova<sup>8</sup>, O. Petukhov<sup>12,d</sup>, J. Pietraszkowski<sup>4</sup>, W. Przygoda<sup>3</sup>, S. Ramos<sup>2</sup>, B. Ramstein<sup>15</sup>, A. Reshetin<sup>12</sup>, P. Rodriguez-Ramos<sup>16</sup>, P. Rosier<sup>15</sup>, A. Rost<sup>5</sup>, A. Sadovsky<sup>12</sup>, P. Salabura<sup>3</sup>, T. Scheib<sup>8</sup>, H. Schuldes<sup>8</sup>, E. Schwab<sup>4</sup>, F. Scozzi<sup>5,15</sup>, F. Seck<sup>5</sup>, P. Sellheim<sup>8</sup>, J. Siebenson<sup>10</sup>, L. Silva<sup>2</sup>, Yu.G. Sobolev<sup>16</sup>, S. Spataro<sup>f</sup>, H. Ströbele<sup>8</sup>, J. Stroth<sup>8,4</sup>, P. Strzempek<sup>3</sup>, C. Sturm<sup>4</sup>, O. Svoboda<sup>16</sup>, M. Szala<sup>8</sup>, P. Tlusty<sup>16</sup>, M. Traxler<sup>4</sup>, H. Tsertos<sup>14</sup>, E. Usenko<sup>12</sup>, V. Wagner<sup>16</sup>, C. Wendisch<sup>4</sup>, M.G. Wiebusch<sup>8</sup>, J. Wirth<sup>10,9</sup>, Y. Zanevsky<sup>7</sup>, P. Zumbrun<sup>4</sup>

(The HADES Collaboration)

<sup>1</sup>*Institute of Physics, Slovak Academy of Sciences, 84228 Bratislava, Slovakia*

<sup>2</sup>*LIP-Laboratório de Instrumentação e Física Experimental de Partículas, 3004-516 Coimbra, Portugal*

<sup>3</sup>*Smoluchowski Institute of Physics, Jagiellonian University of Cracow, 30-059 Kraków, Poland*

<sup>4</sup>*GSI Helmholtzzentrum für Schwerionenforschung GmbH, 64291 Darmstadt, Germany*

<sup>5</sup>*Technische Universität Darmstadt, 64289 Darmstadt, Germany*

<sup>6</sup>*Institut für Strahlenphysik, Helmholtz-Zentrum Dresden-Rossendorf, 01314 Dresden, Germany*

<sup>7</sup>*Joint Institute of Nuclear Research, 141980 Dubna, Russia*

<sup>8</sup>*Institut für Kernphysik, Goethe-Universität, 60438 Frankfurt, Germany*

<sup>9</sup>*Excellence Cluster 'Origin and Structure of the Universe', 85748 Garching, Germany*

<sup>10</sup>*Physik Department E62, Technische Universität München, 85748 Garching, Germany*

<sup>11</sup>*II. Physikalisches Institut, Justus Liebig Universität Giessen, 35392 Giessen, Germany*

<sup>12</sup>*Institute for Nuclear Research, Russian Academy of Science, 117312 Moscow, Russia*

<sup>13</sup>*Institute of Theoretical and Experimental Physics, 117218 Moscow, Russia*

<sup>14</sup>*Department of Physics, University of Cyprus, 1678 Nicosia, Cyprus*

<sup>15</sup>*Institut de Physique Nucléaire, CNRS-IN2P3, Univ. Paris-Sud, Université Paris-Saclay, F-91406 Orsay Cedex, France*

<sup>16</sup>*Nuclear Physics Institute, The Czech Academy of Sciences, 25068 Rez, Czech Republic*

<sup>17</sup>*LabCAF. F. Física, Univ. de Santiago de Compostela, 15706 Santiago de Compostela, Spain*

<sup>a</sup> *also at ISEC Coimbra, Coimbra, Portugal*

<sup>b</sup> *also at ExtreMe Matter Institute EMMI, 64291 Darmstadt, Germany*

<sup>c</sup> *also at Technische Universität Dresden, 01062 Dresden, Germany*

<sup>d</sup> *also at Moscow Engineering Physics Institute (State University), 115409 Moscow, Russia*

<sup>e</sup> *also at Frederick University, 1036 Nicosia, Cyprus*

<sup>f</sup> *also at Dipartimento di Fisica and INFN, Università di Torino, 10125 Torino, Italy*

(Dated: February 18, 2019)

Quantum chromodynamics (QCD) supports the existence of a novel state of strongly interacting matter with temperatures above  $kT = 50$  MeV and densities several times higher than those in nuclei. Such matter can be created in the laboratory as a transient state by colliding heavy ions at relativistic energies. The thermal electromagnetic radiation emitted from the dense stage of these collisions has been used to probe microscopic properties of the produced medium. The spectral distribution of virtual photons – manifesting themselves as di-electron pairs – shows a nearly exponential shape which indeed points to an emitting source of temperature in excess of 70 MeV/ $k$  and to a strong modification of the properties of its constituents. Regarding bulk properties, this medium is similar to the dense matter formed in the final state of a neutron star merger, as apparent from its recent multi-messenger observation.

The motivation to study the properties of transient states of QCD matter (that is strong-interaction matter consisting of hadrons, or quarks and gluons) under extreme conditions of temperature and density has many facets. For instance, the states of QCD matter that filled the universe around  $10\ \mu\text{s}$  after its birth, when quarks and gluons were bound into nucleons, also make up the interior of compact star remnants after core collapse, the neutron stars. The formation of such *cosmic matter* in heavy-ion collisions provides access to studies of the microscopic structure of QCD matter at the femtoscale.

The different phases in which QCD matter may exist depend, as for any other known substance, on state variables like temperature, pressure or chemical potentials. The phase diagram of QCD matter, indicating the conjectured phase boundaries in a graph relating temperature and baryochemical potential ( $\mu_B$ ), is shown in Fig. 1. The situation for symmetric matter ( $\mu_B = 0$ ), where matter is balanced by antimatter, has recently been elaborated in [1]. It is characterized by a crossover between ordinary hadronic matter and a new phase of strongly interacting matter – the quark gluon plasma (QGP). By evaluating QCD with high precision on a lattice it has been found that the crossover occurs at temperatures around  $155\ \text{MeV}/k$  [2, 3], indicated in Fig. 1 by a yellow band. The crossover is quantified by the expectation value of a quantity called scalar quark-antiquark or chiral condensate ( $\langle\bar{q}q\rangle$ ), the order parameter of dynamically broken chiral symmetry, as shown in the figure by blue lines normalized to the expectation value in vacuum. This phenomenon is of fundamental interest since it furnishes a description of chiral symmetry restoration, a symmetry conserving handedness in the strong interaction in the limit of massless quarks. The chiral symmetry is spontaneously broken in vacuum, and, together with the occurrence of a trace anomaly in QCD, responsible for the dynamical generation of mass of all light hadrons and the occurrence of mesons with significantly lower masses representing the Nambu-Goldstone bosons [4].

The conditions for deconfinement in baryon dominated matter (*i.e.*  $\mu_B > 0$ ) are not (yet) accessible by first-principle QCD calculations and are hence not well known. It is currently believed that collisions of heavy ions at energies of a few  $\text{GeV}$  per nucleon do not produce matter under conditions which suffice to free the constituent quarks. Yet, a (partial) restoration of the chiral symmetry is predicted for baryon-rich matter already at moderate temperatures ( $T \leq 100\ \text{MeV}/k$ ) as the chiral condensate is substantially reduced in the fraction of volume occupied by baryons. Hence, a significant modification of the dispersive properties of hadronic states in such a medium is expected.

The experimental approach to explore the QCD matter

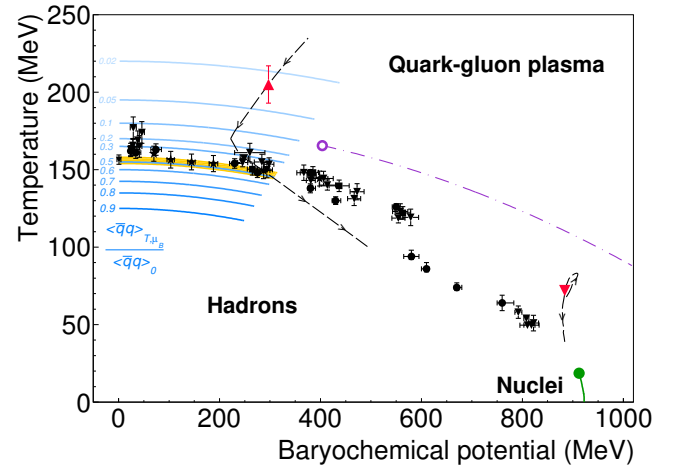


FIG. 1: **The conjectured QCD phase diagram of strongly interacting matter.** The black symbols are the experimentally deduced chemical freeze-out points describing the final state hadron abundances in a statistical hadronization model [1]. The expectation value of the chiral condensate relative to the vacuum as constrained by lattice QCD [2] is depicted as blue contours. The yellow band is the crossover line [3]. The dashed magenta curve shows the conjectured first order phase transition which terminates in a second order QCD critical point, open magenta circle. The red triangle represents the location deduced from the dimuon invariant-mass spectrum measured by the NA60 collaboration [6], while the red inverse triangle is the result of the HADES collaboration, reported here. The black dashed curves indicate the corresponding predicted time evolution of the fireball parameters [7–9]. The solid green curve marks the first order liquid – gas phase transition of nuclear matter [5].

phase diagram is to probe different regions with heavy-ion collisions by varying the collision energy and geometry. As an example, so-called freeze-out conditions ( $T$ ,  $\mu_B$ ), extracted from statistical model fits to the final hadron abundances, have been measured from LHC down to SIS18 energies, as depicted in Fig. 1 (black symbols). They locate the position in the phase diagram where the matter formed in a collision is sufficiently dilute to release its constituent hadrons, which then stream freely to the detectors. These points line up along a narrow band that spans throughout the phase diagram and terminates at vanishing baryochemical potential in the limiting temperature characteristic of the crossover from hadrons to deconfined matter. However, many observational challenges remain like the search for the onset of QGP at high  $\mu_B$ , the location of the QCD critical point, or the study of microscopic properties of matter.

Among all observables dileptons have the distinctive feature of being emitted throughout the whole evolution of the collision zone thus probing the hot and dense phases in a way that no other known observable in heavy-ion collisions can do. They emerge from intermediary virtual photons, immediately decouple from the strong

interaction, and carry additional spectroscopic information encoded in the invariant mass of the virtual photon. The two locations indicated by red triangles in Fig. 1, which were obtained from the spectral distribution of virtual photons, clearly demonstrate the penetrating nature of this radiation. Therefore, dileptons are ideal messengers to probe possible modifications of hadron properties or their disappearance in the medium and thus provide valuable information about the microscopic properties of QCD matter under extreme conditions. In this contribution we report the first observation of dilepton emission from QCD matter at high net-baryon density, which resembles in its properties the matter expected to be formed in binary neutron star mergers.

### Thermal dilepton radiation

Dileptons ( $e^+e^-$ , or  $\mu^+\mu^-$ ) emerge from intermediary virtual photons which directly couple to the electromagnetic current of hadrons. It has been argued that the spectral distribution of dileptons emitted during the early stage of a heavy-ion reaction at ultra-relativistic collision energies should reveal the thermal properties of the medium due to their production in frequent annihilations of quarks and antiquarks [10]. The eight-fold differential emission probability of dileptons from a thermalized source (emissivity) per unit volume and time  $d^4x$ , and in a four-momentum interval  $d^4q$ , is derived from the thermal expectation value of the electromagnetic current-current-correlation function  $\Pi_{em}(M, q; T, \mu_b)$ :

$$\frac{dP}{d^4q d^4x} = -\frac{\alpha^2}{\pi^3 M^2} f^{BE}(q_0, T) \text{Im} \Pi_{em}(M, q; T, \mu_b). \quad (1)$$

Here,  $M \equiv M_{ee}$  is the invariant mass of the lepton pair with four-momentum  $q = (q_0, \vec{q})$ ,  $f^{BE}(q_0, T)$  the thermal Bose-Einstein distribution function characterizing the thermalized medium and  $\alpha$  the fine structure constant. The microscopic properties of the medium are encoded in the imaginary part of the correlator which in turn depends on the baryochemical potential  $\mu_B$  and temperature  $T$ . The dilepton yield observed in an experiment is then given by the space-time integral over the full evolution of the radiating fireball. The strong temperature dependence of the emissivity, nevertheless, favors emission out of the hot and dense stage of the collision. Hence, the yield of radiated thermal dileptons is directly related to the volume and lifetime of the system.

The correlator is well known in the vacuum and observable through the time-reversed process, *i.e.* the annihilation of  $e^+e^-$  into hadronic final states. Its structure suggests a decomposition into a non-perturbative low-mass regime saturated by hadronic resonances with the short-lived  $\rho$  meson playing the dominant role (in accordance with Vector Meson Dominance [11]) and a high-mass regime, where perturbative (partonic) processes start to dominate. By selecting different regions in invariant mass the sensitivity of the experiment can be adjusted to the

hadronic or partonic stage of the fireball evolution.

To evaluate the emissivity of QGP,  $\Pi_{em}$  one has to include any Feynman-graph where  $N$  partons annihilate to a single virtual photon [12]. In case the emitting source has hadronic constituents, the dominant channel producing dileptons is the annihilation of two oppositely charged pions [13] and the imaginary part of the electromagnetic current-current correlator can be represented by the propagator (self-energy) of the  $\rho$  meson [14].

The direct link between the spectral properties of the  $\rho$  meson and dilepton emission qualifies dilepton spectroscopy as ideal tool to probe the in-medium properties of hadrons. According to Eq. 1, modifications of the in-medium  $\rho$  spectral function should be imprinted in the spectral distribution of the dileptons at invariant masses around the vector meson's pole mass. It has been found in [14] that  $\rho$  mesons undergo significant broadening in a hadronic medium giving rise to abundant emission of dileptons in the mass region even below the light vector meson pole mass [15]. The reason for this broadening are contributions to the  $\rho$  meson self-energy arising from the dressing of the pion loop and – most importantly – from its direct coupling to baryons.

The strong modification of the  $\rho$  might be a signal for the onset of chiral symmetry restoration. The (partial) restoration of the dynamically broken chiral symmetry can be demonstrated by calculating the QCD partition function at high temperatures on a lattice for a matter-antimatter symmetric ( $\mu_B = 0$ ) medium [16]. The restoration is governed by the melting of the chiral condensate  $\langle \bar{q}q \rangle$ . This finding is consistent with the conclusion of the Weinberg sum-rules, which state that the spectral properties of the vector meson  $\rho$  and its parity partner the axial-vector  $a_1$  should become degenerate in case of a vanishing  $\langle \bar{q}q \rangle$  expectation value. Such a trend has been demonstrated in [17] based on QCD and Weinberg sum rules and is also supported by a calculation in the Functional Renormalization Group framework [18]. In both cases the degeneracy is realized via strong broadening of the chiral partners. This is a fundamental property derived from current algebra and is therefore expected to hold true also in case of baryonic matter, characterized by a dominance of matter over antimatter ( $\mu_B > 0$ ), not directly accessible by lattice QCD calculations.

According to Eq. 1, in case of weighted correlator ( $\text{Im} \Pi_{em}/M^2$ ) is approximately constant, the dilepton emission rates are determined mostly by the thermal distribution function and ideally suit to extract the temperature of the emitting medium (*thermometer*) [6, 19]. The fact that invariant mass is a Lorentz-invariant quantity removes any bias from this measurement due to Doppler effects caused by the rapid expansion of the fireball.

Due to the penetrating nature of dileptons, their yield in the low-mass ( $0.2 \leq M_{ee}/G\epsilon V/c^2 \leq 0.7$ ) region depends on both the volume  $V$  and the lifetime  $\tau$  of the



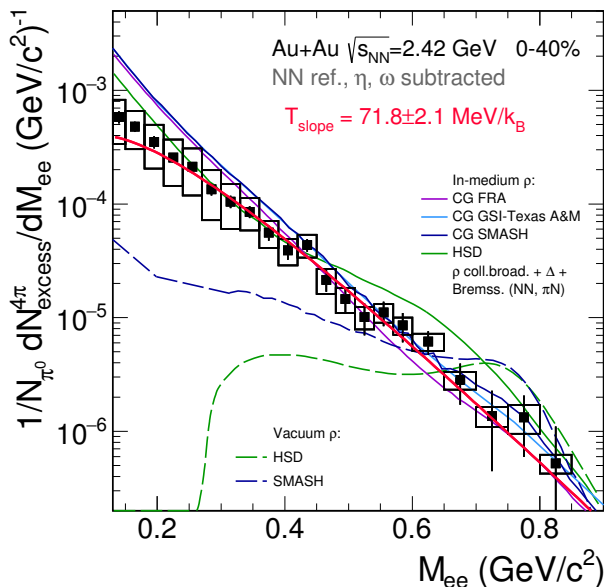


FIG. 3: **Acceptance corrected dilepton excess yield** (black squares) extracted by subtracting  $\eta$ ,  $\omega$  contributions as well as the NN reference normalized to the number of neutral pions. Dashed curves:  $\rho$  (“free” spectral function) contribution from HSD [38] (green) and from SMASH [40] (dark blue) transport model calculations normalized to the respective number of neutral pions. Meaning of the errors as in Fig. 2. Only statistical errors (s.d.) are shown. Solid green curve: incoherent sum of  $\Delta \rightarrow Ne^+e^-$ , NN- and  $\pi N$ -bremsstrahlung and  $\rho$  (collisional broadening scenario) contributions from HSD (multiple  $\Delta$  regeneration is assumed in the model). The dark blue [40], blue [41] and pink [42] curves show the results of three versions of coarse-grained calculations using different concepts for obtaining the local thermal parameters.

The resulting invariant-mass distribution of signal dileptons, derived for the 40% most central Au+Au collisions, are shown in Fig. 2. The signal yield is normalized to the average number of produced charged pions to remove a trivial system-size dependence of the signal-pair yield. The pion multiplicities are found to scale linearly with  $\langle A_{\text{part}} \rangle$ , the mean number of nucleons participating in the formation of the nuclear fireball, for a given collision energy per nucleon. At low invariant masses a clear indication of contribution from three-body  $\pi^0$  Dalitz decays is visible. Above  $M_{ee} \simeq 0.15 \text{ GeV}/c^2$ , the spectrum drops nearly exponentially over almost four orders of magnitude until it runs out of statistics in the vector meson mass region around  $1 \text{ GeV}/c^2$ . Also shown are the expected yields attributed to mesons ( $\pi^0, \eta, \omega, \rho^0, \phi$ ) decaying after they have decoupled from the fireball. Although dileptons radiated from this stage are not considered part of the thermal emission from the fireball, they still contribute to the total reconstructed signal pair yield. Likewise, contributions from baryonic sources (NN bremsstrahlung,  $\Delta$  Dalitz decay) emitted before the fire-

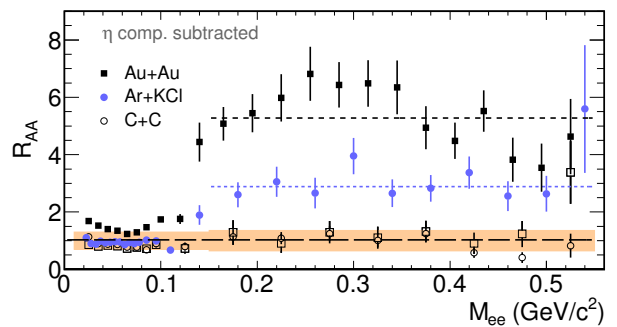


FIG. 4: **Systematics of the  $e^+e^-$  pair yield in A+A collisions attributed to excess radiation.** The ratios ( $R_{AA}$ ) depicted as symbols show the invariant-mass yield for various collision systems A+A [35, 36], per mean number of participating nucleons  $\langle A_{\text{part}} \rangle$  of the respective heavy-ion centrality class, and normalized to the reference yield NN obtained from elementary NN collisions. Horizontal lines mark the corresponding average excess factors (see [37] for details).

ball has formed, which contribute significantly at SIS18 energies [37], are also accounted for. This yield is approximated by the NN reference spectrum (open dark-blue squares) derived from measured p+p and n+p data [33] as

$$\frac{dN_{\text{ref}}^{\text{NN}}}{dM_{ee}} = \left( 0.54 \frac{dN^{\text{pp}}}{dM_{ee}} + 0.46 \frac{dN^{\text{np}}}{dM_{ee}} \right) \langle A_{\text{part}} \rangle, \quad (2)$$

with pre-factors reflecting the isospin composition of the Au+Au collision system. Note that the  $\eta$  contributions has already been removed from the N+N reference since this contribution is taken care of by the mesonic cocktail, *i.e.* conventional sources. While the Au+Au signal-pair yield and NN reference agree in the  $\pi^0$ -Dalitz region ( $M_{ee} < 0.15 \text{ GeV}/c^2$ ) as expected, they differ strikingly for masses  $M_{ee} > 0.15 \text{ GeV}/c^2$ . In this region, the yield from Au+Au collisions exceeds the NN reference and mesonic cocktail substantially, clearly indicating the presence of excess radiation originating from the dense hadronic medium.

### Excess radiation

To isolate this excess radiation we first subtract the contributions from conventional sources (*cf.* Eq. (2) and Fig. 2). We further apply a mass dependent acceptance correction factor in analogy to the efficiency correction explained in the Methods Section, but this time relating simulated pairs in the acceptance to all simulated pairs. The resulting dilepton excess radiation is presented in Fig. 3 and exhibits a near-exponential fall-off. A fit of  $dN/dM_{ee} \propto (M_{ee})^{3/2} \times \exp(-M_{ee}/T)$  (black-body spectral distribution) to the data gives a satisfactory overall description of the distribution and yields an inverse slope parameter of  $kT = 71.8 \pm 2.1 \text{ MeV}$  ( $\chi^2/\text{ndf} = 13.2/17$ ). This fit is justified, because to a good approximation ( $\text{Im} \Pi_{em}/M^2$ ) is constant and the spectrum dominated

by the thermal Bose-Einstein distribution function (*c.f.* Eq. (1)). The integrated excess yield in the invariant-mass window  $0.3 \leq M_{ee}/\text{GeV}/c^2 \leq 0.7$  is found to be  $N_{\text{excess}}^{4\pi} = (1.07 \pm 0.06^{\text{stat}} \pm 0.2^{\text{syst}}) \times 10^{-4}$  for the 40% most central events. For the Au+Au collisions class presented in Fig. 2 with  $\langle A_{\text{part}} \rangle = 193.3$ , the excess outshines the conventional sources by an average factor of  $5.7 \pm 0.3^{\text{stat}}$ . This excess reaches a factor of  $\sim 12$  if the 10% most central events are selected, reflecting the number of virtual  $\rho$  generations during the fireball evolution. This clearly signals a qualitative change in the nature of radiating sources, immanent to heavier collision systems.

The dynamics of heavy-ion collisions at bombarding energies of a few GeV per nucleon have successfully been addressed by microscopic transport models [38–40]. However, for the description of dilepton emission, these calculations usually do not treat modifications of the  $\rho$  meson explicitly on the level of in-medium spectral functions. As can indeed be seen in Fig. 3, transport calculations assuming a “free”  $\rho$  spectral function (HSD, SMASH) [38, 40] feature a clear bump around  $M_{ee} = 0.7 \text{ GeV}/c^2$  which is obviously not observed in the experimental data. Note also that the vacuum spectral function used in HSD differs from the one in SMASH due to a different implementation of the  $\rho$  production mechanism. The agreement between transport model calculations and data can, however, be improved assuming a strong *collisional broadening* of the  $\rho$  spectral function as demonstrated in case of the Hadron String Dynamics transport model (HSD). Furthermore, in HSD, most of the yield at the lower invariant masses is saturated by the contribution from an incoherent summation over  $\Delta$ ,  $\pi$ N- and NN bremsstrahlung processes.

On the other hand, the excess radiation can be satisfactorily described assuming thermal emission rates folded with a space-time evolution of the fireball derived from coarse-grained microscopic transport calculations (UrQMD, SMASH) [40–42] (*c.f.* section about thermal radiation). The structureless excess yield indicates a strong medium modification of the  $\rho$  meson likely induced by the high baryon density in the environment. This is a remarkable observation as model calculation, based on the same in-medium spectral function, precisely reproduce the excess radiation measured at much higher collision energies. Despite of earlier concerns [43] about the applicability of this approach at low beam energies, the calculation agrees well with data in the region  $M_{ee} > 0.3 \text{ GeV}/c^2$  but systematically overshoots the measurement for small invariant masses, an observation which needs to be further investigated.

Further evidence for the existence of thermal radiation is obtained from studying the system size dependence of the dilepton radiation. In Fig. 4 we present yields of signal-pairs obtained in A+A collisions divided by the respective expectation from conventional sources for three

different collision systems according to

$$R_{AA} = \frac{1}{\langle A_{\text{part}}^{AA} \rangle} \frac{dN^{AA}}{dM_{ee}} \left( \frac{dN^{NN}}{dM_{ee}} \right)^{-1}. \quad (3)$$

The excess is observable once the invariant mass exceeds the  $\pi^0$  Dalitz region. While for C+C collision system, the ratio is still consistent with unity within systematic uncertainties, the radiation is enhanced by an average factor of three in case of Ar+KCl collisions. The strongest excess is observed for Au+Au collisions. A comparison of coarse-grained transport model calculations with data in the moderately heavy Ar+KCl collision system,  $\langle A_{\text{part}} \rangle = 38.5$ , also demonstrates the limitations of using vacuum properties for the hadrons: agreement with data is indeed achieved only with explicit in-medium spectral functions [40, 42, 44].

These results demonstrate that although at the beam energies considered here only about 10% of the charged particles in the final state are mesons (chiefly pions), we nevertheless observe a strong excess of the dileptons. This yield is way beyond what is expected from known sources and its spectral distribution is well described by assuming decays of in-medium  $\rho$  mesons. The data supports the assumption of a strong broadening which can be connected to partial restoration of the dynamically broken chiral symmetry.

### Prospects

The recently observed gravitational wave signals of a binary neutron star merger event opened a new era in multi-messenger astronomy and possibly also a new avenue to connect stellar structures to the properties of the elementary building blocks of matter. Sophisticated model calculations show that post-merger neutron star configurations can develop a heated shell around the dense remnant core. In particular, they suggest that temperatures of 50 – 80 MeV and densities of around two times nuclear ground state densities might be reached [45, 46]. To recall, the average temperature of the radiating fireball formed in Au+Au collision at  $\sqrt{s_{NN}} = 2.42 \text{ GeV}$  was found to be  $71.8 \pm 2.1 \text{ MeV}$ , with densities of up to three times normal nuclear matter density reached in the central region of the fireball.

In Fig. 5 (bottom row) shows results from a simulation based on microscopic transport theory of the reaction investigated in this paper. The panels show snapshots of the density evolution in the equatorial plane for characteristic stages of the reaction. They are conjoined with respective snapshots obtained from a simulation of a binary neutron star merger (top row). While the space and time scales differ by typically twenty orders of magnitude, yet the matter properties in each system show striking similarities *w.r.t.* density and temperature. The relation pressure – energy density – temperature – density, condensed in the equation-of-state, is of paramount importance for modeling merger/collision events. However,

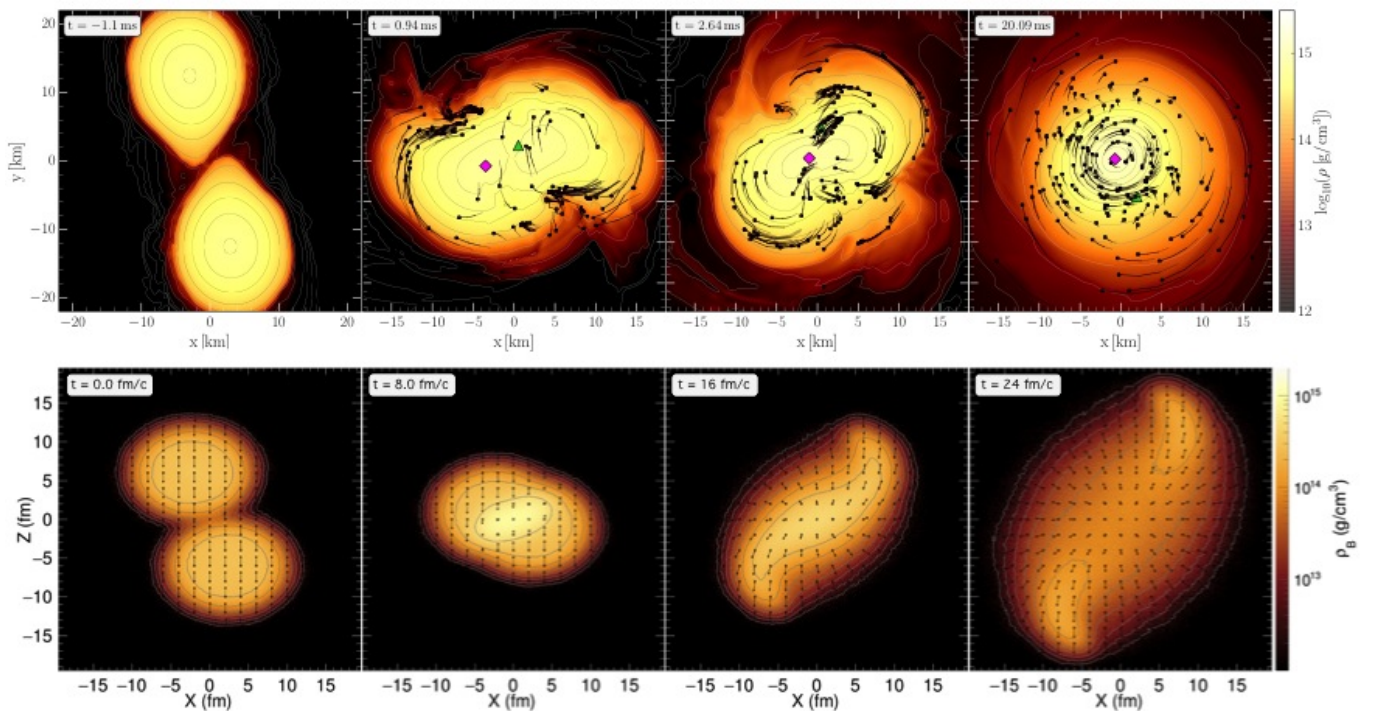


FIG. 5: **Simulations of nuclear matter in collisions yielding extreme conditions of densities (see color code bars) and temperatures:** Two merging neutron stars (top row) and two colliding gold nuclei (bottom row). While the same densities and temperatures are achieved, the displayed space and time scales are vastly different: kilometer for the neutron star merger simulation and femtometer in case of the heavy-ion collision. Likewise, the collision events differ in duration by 20 orders of magnitude. Top row: Simulation of a binary neutron star encounter of two neutron stars of equal masses with  $1.35 M_{\odot}$  each finally merging into a single compact object [46] (size of about 10 km in diameter, densities of up to 5 times saturation density and temperatures reaching as high as 20 MeV). The matter is heated in the overlap zone and a super heated region surrounding the dense core is created about 20 ms after first contact with densities of about 2 times saturation density and temperatures of up to 75 MeV. The two neutron stars revolve (clockwise) around a common center-of-mass. The green triangle marks the maximum value of the temperature while the magenta diamond indicates the maximum of the density. Bottom row: Time evolution of the energy density achieved in a non-central collision of two gold nuclei at an energy of 2.42 GeV per colliding nucleon pair. The z-axis corresponds to the beam axis of the Au+Au collision. Densities reach up to 3 times normal matter density and temperatures of up to 80 MeV. The simulation is based on [9]. Arrows depict local fluid flow velocities.

not much is known about the equation-of-state of such forms of matter. Among further quantities of high relevance are viscosities and conductivities, which are linked to real and virtual photon emissivities through a common theoretical basis. Therefore, the observation of thermal (virtual) photon emission off dense baryon matter in relativistic heavy-ion collisions serves as a benchmark for accessing other bulk properties.

To advance our understanding of the emissivity of strong-interaction matter under extreme conditions of temperature and density it is important to extend such measurements to different collision energies. HADES will continue the investigations with measurements by employing the upgraded installation of the detector providing substantially increased statistics then enabling access to the continuum radiation around  $M_{ee} \geq 1 \text{ GeV}/c^2$  already at SIS energies. Experiments at RHIC and the LHC with improved setups will scrutinize the conditions of matter at small baryon chemical potential. Fu-

ture dilepton measurements at FAIR, SPS, NICA and J-PARC-HI facilities will operate at interaction rates a factor 100 higher than present facilities. They will enable multi-differential analyses with precision on the percent level and thus help to scrutinize our knowledge of the chiral symmetry restoration in hot and dense matter and the QCD phase structure at high baryon chemical potential.

The collaboration gratefully acknowledges the support by PTDC/FIS/113339/2009 LIP Coimbra, NCN grant 2013/10/M/ST2/00042 SIP JUC Cracow, Helmholtz Alliance HA216/EMMI GSI Darmstadt, VH-NG-823, Helmholtz Alliance HA216/EMMI TU Darmstadt, 283286, 05P12CRGHE HZDR Dresden, Helmholtz Alliance HA216/EMMI, HIC for FAIR (LOEWE), GSI F&E Goethe-Universität, Frankfurt VH-NG-330, BMBF 06MT7180 TU München, Garching BMBF:05P12RGGHM JLU Giessen, Giessen UCY/3411-23100, University Cyprus CNRS/IN2P3 IPN Orsay, Orsay, MEYS LM2015049,

- [1] A. Andronic, P. Braun-Munzinger, K. Redlich and J. Stachel, “Decoding the phase structure of QCD via particle production at high energy,” *Nature* **561** (2018) no.7723, 321.
- [2] S. Borsanyi *et al.* [Wuppertal-Budapest Collaboration], “Is there still any  $T_c$  mystery in lattice QCD? Results with physical masses in the continuum limit III,” *JHEP* **1009**, 073 (2010).
- [3] A. Bazavov *et al.*, “Chiral crossover in QCD at zero and non-zero chemical potentials,” arXiv:1812.08235 [hep-lat].
- [4] C. D. Roberts, “Perspective on the origin of hadron masses,” *Few Body Syst.* **58**, no. 1, 5 (2017).
- [5] S. Floerchinger and C. Wetterich, “Chemical freeze-out in heavy ion collisions at large baryon densities,” *Nucl. Phys. A* **890-891**, 11 (2012).
- [6] H. J. Specht [NA60 Collab.], “Thermal Dileptons from Hot and Dense Strongly Interacting Matter,” *AIP Conf. Proc.* **1322**, 1 (2010).
- [7] R. Rapp, “Hadro chemistry and evolution of (anti-) baryon densities at RHIC,” *Phys. Rev. C* **66**, 017901 (2002).
- [8] J. N. Guenther, R. Bellwied, S. Borsanyi, Z. Fodor, S. D. Katz, A. Pasztor, C. Ratti and K. K. Szab, “The QCD equation of state at finite density from analytical continuation,” *Nucl. Phys. A* **967**, 720 (2017).
- [9] S. A. Bass *et al.*, “Microscopic models for ultrarelativistic heavy ion collisions,” *Prog. Part. Nucl. Phys.* **41**, 255 (1998).
- [10] E. V. Shuryak, “Quark-Gluon Plasma and Hadronic Production of Leptons, Photons and Psions,” *Phys. Lett.* **78B**, 150 (1978).
- [11] N. M. Kroll, T. D. Lee and B. Zumino, “Neutral Vector Mesons and the Hadronic Electromagnetic Current,” *Phys. Rev.* **157**, 1376 (1967).
- [12] L. D. McLerran and T. Toimela, “Photon and Dilepton Emission from the Quark - Gluon Plasma: Some General Considerations,” *Phys. Rev. D* **31**, 545 (1985).
- [13] C. Gale and J. I. Kapusta, “Dilepton radiation from high temperature nuclear matter,” *Phys. Rev. C* **35**, 2107 (1987).
- [14] R. Rapp and J. Wambach, “Chiral symmetry restoration and dileptons in relativistic heavy ion collisions,” *Adv. Nucl. Phys.* **25**, 1 (2000).
- [15] R. D. Pisarski, “Phenomenology of the Chiral Phase Transition,” *Phys. Lett.* **110B**, 155 (1982).
- [16] H. T. Ding, O. Kaczmarek and F. Meyer, “Thermal dilepton rates and electrical conductivity of the QGP from the lattice,” *Phys. Rev. D* **94**, no. 3, 034504 (2016).
- [17] P. M. Hohler and R. Rapp, “Is  $\rho$ -Meson Melting Compatible with Chiral Restoration?,” *Phys. Lett. B* **731**, 103 (2014)
- [18] C. Jung, F. Rennecke, R. A. Tripolt, L. von Smekal and J. Wambach, “In-Medium Spectral Functions of Vector- and Axial-Vector Mesons from the Functional Renormalization Group,” *Phys. Rev. D* **95**, no. 3, 036020 (2017)
- [19] R. Rapp and H. van Hees, “Thermal Dileptons as Fireball Thermometer and Chronometer,” *Phys. Lett. B* **753**, 586 (2016).
- [20] U. W. Heinz and K. S. Lee, “The rho peak in the dimuon spectrum as a clock for fireball lifetimes in relativistic nuclear collisions,” *Phys. Lett. B* **259**, 162 (1991).
- [21] H. W. Barz, B. L. Friman, J. Knoll and H. Schulz, “Production of phi, rho and omega mesons in the hadronization of a quark - gluon plasma,” *Phys. Lett. B* **254**, 315 (1991).
- [22] D. Adamova *et al.* [CERES/NA45 Collab.], “Enhanced production of low mass electron pairs in 40-A-GeV Pb - Au collisions at the CERN SPS,” *Phys. Rev. Lett.* **91**, 042301 (2003).
- [23] G. Agakishiev *et al.* [CERES/NA45 Collab.], “Low mass e+ e- pair production in 158/A-GeV Pb - Au collisions at the CERN SPS, its dependence on multiplicity and transverse momentum,” *Phys. Lett. B* **422**, 405 (1998).
- [24] R. Arnaldi *et al.* [NA60 Collab.], “First measurement of the rho spectral function in high-energy nuclear collisions,” *Phys. Rev. Lett.* **96**, 162302 (2006).
- [25] A. Adare *et al.* [PHENIX Collab.], “Dielectron production in Au+Au collisions at  $\sqrt{s_{NN}}=200$  GeV,” *Phys. Rev. C* **93**, 014904 (2016).
- [26] L. Adamczyk *et al.* [STAR Collab.], “Measurements of Dielectron Production in Au+Au Collisions at  $\sqrt{s_{NN}} = 200$  GeV from the STAR Experiment,” *Phys. Rev. C* **92**, 024912 (2015).
- [27] J. Adam *et al.* [STAR Collaboration], “Measurements of Dielectron Production in Au+Au Collisions at  $\sqrt{s_{NN}}= 27, 39,$  and 62.4 GeV from the STAR Experiment,” arXiv:1810.10159 [nucl-ex].
- [28] M. Herrmann, B. L. Friman and W. Nörenberg, “Properties of rho mesons in nuclear matter,” *Nucl. Phys. A* **560**, 411 (1993).
- [29] G. Chanfray and P. Schuck, “The Rho meson in dense matter and its influence on dilepton production rates,” *Nucl. Phys. A* **555**, 329 (1993).
- [30] W. Peters, M. Post, H. Lenske, S. Leupold and U. Mosel, “The Spectral function of the rho meson in nuclear matter,” *Nucl. Phys. A* **632**, 109 (1998).
- [31] W. K. Wilson *et al.* [DLS Collab.], “Inclusive dielectron cross-sections in p + p and p + d interactions at beam energies from 1.04-GeV to 4.88-GeV,” *Phys. Rev. C* **57**, 1865 (1998).
- [32] R. J. Porter *et al.* [DLS Collab.], “Dielectron cross-section measurements in nucleus-nucleus reactions at 1-A/GeV,” *Phys. Rev. Lett.* **79**, 1229 (1997).
- [33] G. Agakishiev *et al.* [HADES Collab.], “Origin of the low-mass electron pair excess in light nucleus-nucleus collisions,” *Phys. Lett. B* **690**, 118 (2010).
- [34] J. Adamczewski-Musch *et al.* [HADES Collab.], “Analysis of the exclusive final state  $npe^+e^-$  in quasi-free np reaction,” *Eur. Phys. J. A* **53**, 149 (2017).
- [35] G. Agakishiev *et al.* [HADES Collab.], “Dielectron production in C-12+C-12 collisions at 2-AGeV with HADES,” *Phys. Rev. Lett.* **98**, 052302 (2007).
- [36] G. Agakishiev *et al.* [HADES Collab.], “Study of dielectron production in C+C collisions at 1-A-GeV,” *Phys. Lett. B* **663**, 43 (2008).
- [37] G. Agakishiev *et al.* [HADES Collab.], “Dielectron production in Ar+KCl collisions at 1.76A GeV,” *Phys. Rev. C* **84**, 014902 (2011).
- [38] E. L. Bratkovskaya *et al.*, “System size and energy dependence of dilepton production in heavy-ion collisions at 1-2 GeV/nucleon energies,” *Phys. Rev. C* **87**, 064907 (2013).
- [39] J. Weil, H. van Hees and U. Mosel, “Dilepton production in proton-induced reactions at SIS energies with the GiBUU transport model,” *Eur. Phys. J. A* **48**, 111 (2012). Erratum: [*Eur. Phys. J. A* **48**, 150 (2012)]
- [40] J. Staudenmaier, J. Weil, V. Steinberg, S. Endres and H. Petersen, “Dilepton production and resonance properties within a new hadronic transport approach in the context of the GSI-HADES experimental data,” *Phys. Rev. C* **98**, no. 5, 054908 (2018).
- [41] T. Galatyuk, P. M. Hohler, R. Rapp, F. Seck and J. Stroth, “Thermal Dileptons from Coarse-Grained Transport as Fireball Probes at SIS Energies,” *Eur. Phys. J. A* **52**, 131 (2016).
- [42] S. Endres, H. van Hees, J. Weil and M. Bleicher, “Dilepton production and reaction dynamics in heavy-ion collisions at SIS energies from coarse-grained transport simulations,” *Phys. Rev. C* **92**, 014911 (2015).
- [43] A. Lang, B. Blaettel, V. Koch, K. Weber, W. Cassing and U. Mosel, “Local thermodynamic properties and equilibration in relativistic heavy ion collisions,” *Phys. Lett. B* **245**, 147 (1990).
- [44] F. Seck, T. Galatyuk, R. Rapp and J. Stroth, “Thermal dileptons as QCD matter probes at SIS,” *J. Phys. Conf. Ser.* **1024**, 012011 (2018).
- [45] A. Bauswein, S. Goriely and H.-T. Janka, “Systematics of dy-

namical mass ejection, nucleosynthesis, and radioactively powered electromagnetic signals from neutron-star mergers,” *Astrophys. J.* **773**, 78 (2013).

- [46] E. R. Most, L. J. Papenfort, V. Dexheimer, M. Hanauske, S. Schramm, H. Stöcker and L. Rezzolla, “Signatures of quark-hadron phase transitions in general-relativistic neutron-star mergers,” arXiv:1807.03684 [astro-ph.HE]

## Methods

### The HADES apparatus

As shown in the supplementary Figs. S1 and S2, the HADES detector [50] features a six-coil super-conducting toroidal magnet providing very good acceptance for charged particles emitted from the collision zone mostly at polar angles between  $18^\circ$  and  $85^\circ$ . Each sector of the resulting hexagonal detector volume is equipped with four planes of Mini-Drift Chambers (MDC), two in front of and two behind the magnetic field region. The tracking section is followed by a time-of-flight (TOF) system, composed of plastic scintillator strips covering angles above  $45^\circ$  and a resistive plate detector (RPC), followed by an electromagnetic pre-shower detector (Shower), covering the region below.

The field-free region surrounding the target holds a Ring-Imaging Cherenkov (RICH) detector designed to selectively detect electrons and positrons by their Cherenkov emission (yellow lines). Ultra-thin and radiation-hard segmented diamond detectors are installed in the beam line up-stream of the target to provide precise time-zero information and to synchronize the reaction trigger. The setup is complemented with a large-area scintillator hodoscope, placed 7 m down-stream, which is used to provide additional event characterization, like centrality and reaction plane of each registered collision.

### Event selection

Au+Au collisions investigated in this analysis were recorded by requiring a trigger of at least 20 hits in the TOF detector system. This condition selects the class of the 40% most central Au+Au collisions, corresponding to reaction impact parameters  $b \leq 9.3$  fm. The centrality classes are extracted from a detailed comparison of the observed charged-particle multiplicity distribution in HADES with both a Glauber Monte Carlo model and microscopic transport model calculations of the collision system [51]. The event sample used in the dilepton analysis amounts in total to  $2.6 \times 10^9$  Au+Au collisions. Electron and positron track candidates were searched for and isolated by first matching (in space and time) high-quality particle tracks reconstructed in the MDC planes with a corresponding unique hit in the time-of-flight detectors. Next,  $e^-$  and  $e^+$  were identified by requiring a matching ring pattern in the hadron-blind RICH detector. Finally all possible pair combinations were formed, opposite-sign and like-sign, and the corresponding lepton pair 4-momenta were calculated.

### Reconstruction of pure electron/positron samples

To further improve the purity of  $e^+$  and  $e^-$  candidates, alternative approaches were adopted, each of them trading efficiency vs. purity in different ways. In the standard approach, a series of independent conditions on the correlation of the particle velocity and momentum, the

magnitude of the Shower signal and a refined declination of the RICH ring was required, as described in [37, 50]. The second approach (*ring-finder*) combined these observables and further parameters defining the ring quality into an input vector of an artificial neural network (implemented in the Root toolkit for multivariate data analysis [52]). Signal and background samples were defined either by selecting high-purity samples from data or based entirely on full Monte Carlo simulations employing dedicated digitizers to model the true detector response. A third procedure also used a neural network but did not require an identified ring in the RICH detector. Rather, the region of interest on the RICH photo detector plane was searched for signatures of a ring (*back tracking*). The intersection of the track with the mirror was determined and the location of the expected ring center on the photo detector plane was then calculated making use of the optical properties of the RICH. The latter procedure has in particular advantages in case of touching or overlapping rings, typical for pairs with opening angles  $\alpha_{ee} < 4^\circ$ . In the final step of data processing, all identified  $e^-$  and  $e^+$  candidates of a given event were combined to “neutral” (unlike-sign) pairs. Most of these pairs, however, represent random combinations (*i.e.* they do not stem from the same virtual photon) and form the combinatorial background (CB).

### Extraction of the pair signal

The dilepton spectrum was finally extracted by subtracting from the differential unlike-sign pair yield ( $N^{+-}$ ) the distribution of the CB. To estimate the CB we employed the same-event like-sign method as  $N^{\text{CB}} = 2\kappa (N^{++} \times N^{--})^{0.5}$ , where the factor  $\kappa$  accounts for a charge asymmetry of the spectrometer acceptance and reconstruction. The  $\kappa$  factor was computed with the help of the event-mixing method using the relation  $\kappa = N_{\text{mix}}^{+-} / (N_{\text{mix}}^{++} \times N_{\text{mix}}^{--})^{0.5}$ . The event-mixed distributions generated from data and Monte Carlo simulation coincide, which benchmarks the correctness of efficiency modeling in the HADES Monte Carlo. For invariant masses  $M_{ee} > 0.3$  GeV/ $c^2$ , where the statistics of the like-sign same-event background is limited, the mixed-event unlike-sign yield, scaled to the integral of the like-sign yield, was used. For invariant masses below 0.3 GeV/ $c^2$ , the same-event method was taken to properly account for correlated background. The finally obtained invariant mass distributions for all pairs ( $N^{+-}$ ) and background pairs (CB) are shown in the supplementary Fig. S3 for the *back tracking* analysis procedure. The raw signal emerges after subtracting  $N^{\text{CB}}$  from the  $N^{+-}$ . Also depicted is the signal-to-background ratio ( $S/B$ ), which reaches a minimum of 10% around  $M_{ee} \simeq 0.25$  GeV/ $c^2$ . The signal spectrum contains 190,000 and 20,000  $e^+e^-$  in the mass region below and above 0.15 GeV/ $c^2$ , respectively.

### Correction for detector inefficiency

The signal distribution was further corrected for inefficiencies due to the detector response and inactive regions within the acceptance of the spectrometer (coil region, fiducial areas). For that, individually simulated  $e^-$  and  $e^+$  tracks were generated in the acceptance and embedded into real events on an event-by-event basis. They were then reconstructed using the full analysis and reconstruction chain. For each three-dimensional phase space bin  $d^3p_{lab} \propto dpd\theta d\phi$  the ratio of the number of reconstructed leptons over those accepted within the HADES geometry was derived (single-lepton efficiency matrix). The pair invariant-mass signal was then corrected based on the single-lepton efficiency  $\epsilon^\pm(p, \theta, \phi)$  by deriving a correction vector as  $N_i^{\text{corr}}(M) = N_i(M)/\hat{\epsilon}_i$  with

$$\hat{\epsilon}_i = \hat{\epsilon}(M_i) = \frac{\int_{M_i}^{M_i+\Delta_i} \sum_n \epsilon_n^+ \epsilon_n^- \delta(M - M_n) dM}{\int_{M_i}^{M_i+\Delta_i} \sum_n \delta(M - M_n) dM}, \quad (4)$$

where the sum is running over several sets ( $n$ ) of simulated  $e^+e^-$  using various cocktail generators realized in the Pluto simulation package [56],  $\epsilon_n^\pm = \epsilon^\pm(p_n, \theta_n, \phi_n)$ ,  $M_n$  is the invariant mass of the simulated pair, and  $M_i$  and  $\Delta_i = M_{i+1} - M_i$  are the position and width of the  $i$ th mass bin, respectively. The used source cocktail contained  $\pi^0$ ,  $\eta$  and  $\omega$ -Dalitz decays, as well as a thermal  $\rho$  contribution. The systematic uncertainty in the efficiency determination due to our particular choice of cocktail was evaluated by alternatively taking dileptons from the microscopic transport code HSD. Differences in pair efficiency were found to be below 7% and smooth as function of invariant mass (*c.f.* the discussion of systematic errors below).

### Hadron decay cocktail

The different meson multiplicities were determined as follows: (i) for the  $\pi^0$  the charged pion multiplicities were used, *i.e.*  $N_{\pi^0} \equiv \frac{1}{2}(N_{\pi^-} + N_{\pi^+}) = 8.65 \pm 0.39^{\text{syst}} \pm 0.35^{\text{extrap}}$ , (ii) the  $\eta$  multiplicity was obtained by an analysis of the same data set using the photon conversion method as  $N_\eta = 0.11 \pm 0.01^{\text{syst}} \pm 0.03^{\text{syst}} \pm 0.01^{\text{extrap}}$ ; this value is consistent with the interpolated TAPS measurement [57], (iii) the  $\phi$  multiplicity was reconstructed via the  $K^+K^-$  decay channel as  $N_\phi = (9.9 \pm 2.4^{\text{syst}} \pm 1.0^{\text{syst}} \pm 0.5^{\text{extrap}}) \times 10^{-5}$  [58], and (iv) the  $\omega$  multiplicity  $N_\omega = (9.9 \pm 3.5) \times 10^{-3}$  was determined by fitting the acceptance corrected invariant mass spectrum itself in the region  $M_{ee} = 0.4 - 1 \text{ GeV}/c^2$  with the sum of a Gaussian and an exponential.

### Estimation of systematic errors

Systematic uncertainties are shown as boxes and are generally larger than statistical ones. They are due to variations observed in various analysis steps, namely:

- Subtraction of the combinatorial background brings an uncertainty of  $0.02 \times \text{B/S}$ . This is the largest contribution to the systematic error.

- Calculating the single lepton efficiency by embedding simulated electrons and positrons either into UrQMD events or into real events. This contribution was estimated bin-by-bin in pair observables and is smaller than 2%.
- Using different models to calculate one-dimensional efficiency and acceptance corrections. This contribution is calculated bin-by-bin in pair observables and brings 4% at maximum in the case of efficiency correction and 7% at maximum in the case of efficiency and acceptance correction combined.
- Self-consistency check of the efficiency correction allows to estimate the uncertainty of the correction procedure to  $\leq 10\%$ . It reflects the difference between the reconstructed distributions after applying all corrections and the simulated original spectra.
- Normalization to the number of  $\pi^0$  contributes with 10% uncertainty.
- The uncertainty of the  $\eta$  yield, calculated bin-by-bin, is 5% at maximum. This uncertainty is included only for those spectral bins where the  $\eta$  was actually subtracted.
- Uncertainty of the measured NN reference spectra. This contribution, calculated bin-by-bin, is 20% in the  $\pi^0$  region and besides that has a maximum of 10% at an invariant mass around  $0.5 \text{ GeV}/c^2$  where the difference between the reference and the Au+Au spectra is smallest. This uncertainty is included only for those spectra where the reference was actually subtracted.

All systematic uncertainties were finally added in quadrature to obtain the total systematic uncertainty as a function of  $M_{ee}$ .

### Data availability

All data shown in figures are (will be) publicly available from HEPdata (<https://hepdata.net/>).

### Code availability

The HADES raw data has been analyzed with the ROOT-based customized reconstruction software HYDRA and stored in data summary files.

### Role of individual authors in the project

All authors have contributed to the publication, being variously involved in the design and the construction of the detectors, in writing software, calibrating subsystems, operating the detectors and acquiring data, and finally analyzing the processed data. The HADES Collaboration members discussed and approved the scientific results. The manuscript was prepared by a subgroup of authors appointed by the collaboration and subject to an internal collaboration-wide review process. All

authors reviewed and approved the final version of the manuscript.

### Supplementary information

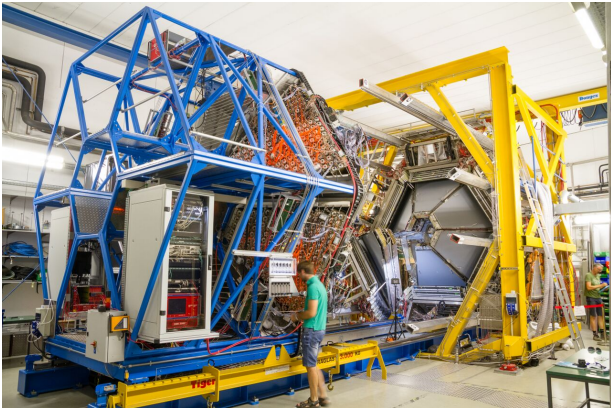


FIG. 1: Photograph of the HADES detector system. The configuration is optimized to dig out  $e^+e^-$  pairs from a huge back-ground generated by other charged particles.

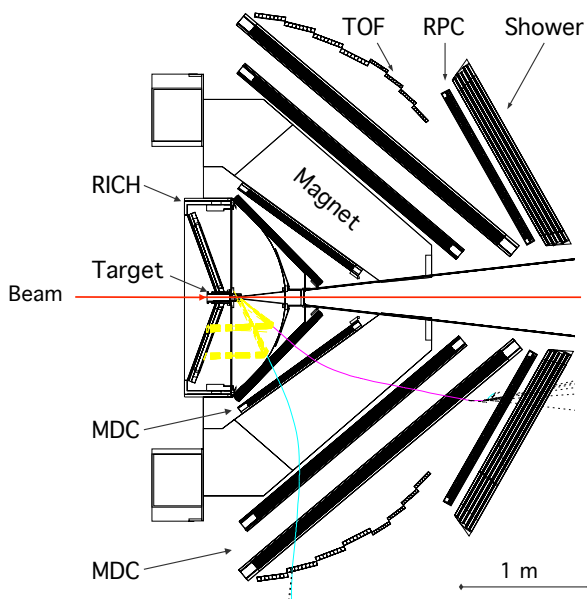


FIG. 2: Cross sectional view of the detector system. See Methods for an explanation of the components. The cyan and magenta curves depict trajectories of an electron (cyan) and a positron (magenta) stemming from a virtual photon. In Supplementary Fig. 1, only the rear sides of the TOF and RPC components are visible and an electromagnetic calorimeter is visible meant to replace the Shower detector in future measurement campaigns.

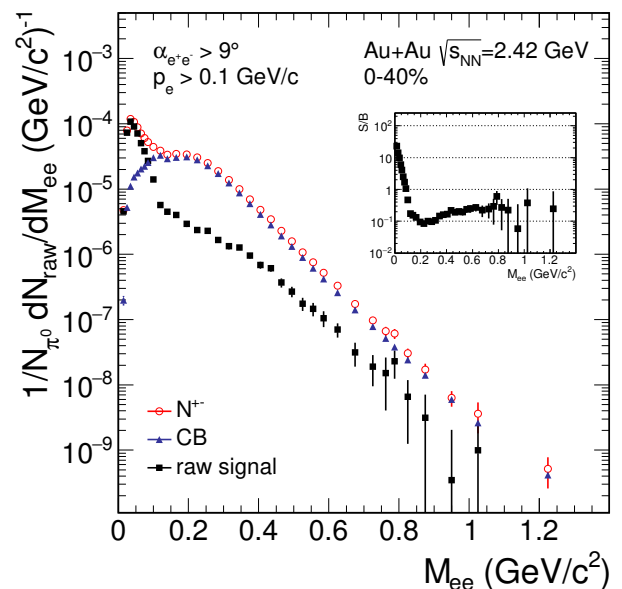


FIG. 3: Raw (before efficiency correction) dielectron invariant-mass distributions obtained from the 40% most central Au+Au collisions at  $\sqrt{s_{NN}} = 2.42$  GeV. Red circles: all same-event unlike-sign combinations ( $N^{+-}$ ), blue triangles: the calculated combinatorial background (CB), black squares: the raw signal ( $N^{+-} - N^{CB}$ ). Statistical errors (s.d.) of the measured yields are shown as vertical bars. Insert shows the signal-over-CB ratio versus invariant mass.

- [50] G. Agakishiev *et al.* [HADES Collab.], *Eur. Phys. J. A* **41**, 243 (2009).
- [51] J. Adamczewski-Musch *et al.* [HADES Collab.], *Eur. Phys. J. A* **54**, 85 (2018).
- [52] A. Hocker *et al.*, *PoS ACAT*, 040 (2007).
- [53] S. Harabasz, PhD Thesis, Technical University of Darmstadt and Jagiellonian University Cracow (2017).
- [54] P. Sellheim, PhD Thesis, Goethe-University Frankfurt (2017).
- [55] C. Behnke, PhD Thesis, Goethe-University Frankfurt (2017).
- [56] I. Fröhlich *et al.*, *J. Phys. Conf. Ser.* **219**, 032039 (2010).
- [57] R. Averbek *et al.* [TAPS Collab.], *Z. Phys. A* **359**, 65 (1997).
- [58] J. Adamczewski-Musch *et al.* [HADES Collab.], *Phys. Lett. B* **778**, 403 (2018).